Matter

CellPress

Article

Dynamic and Programmable Cellular-Scale Granules Enable Tissue-like Materials

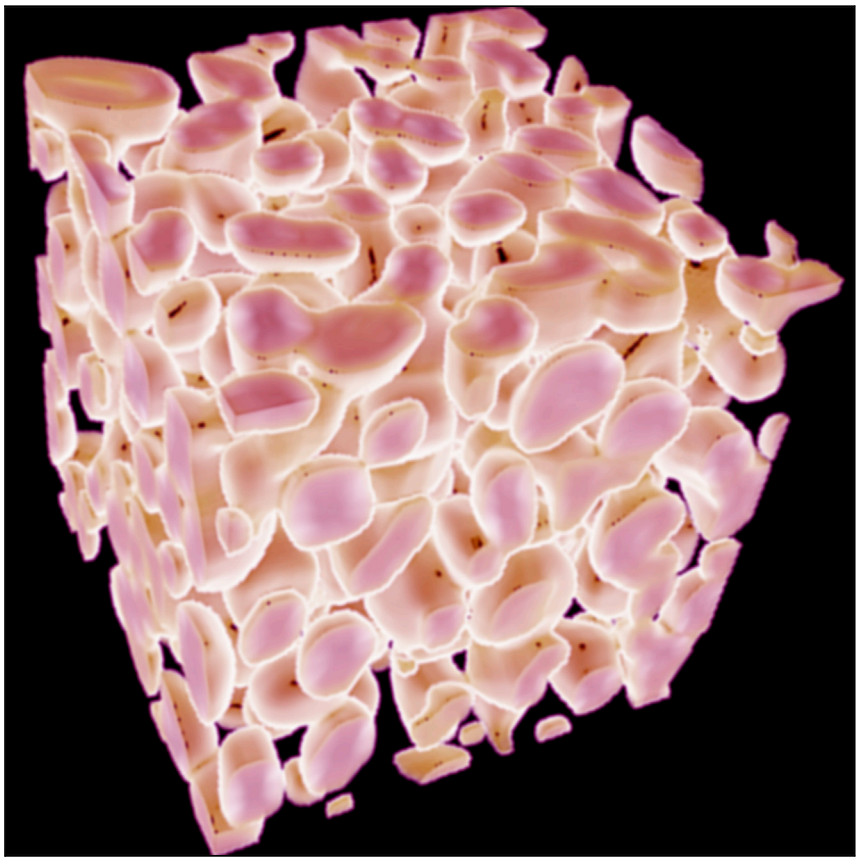

Living tissues contain dense cellular ensembles and extracellular matrices (ECMs). Despite extensive efforts in the biomimetics field to develop ECM-like synthetic polymeric networks, a synthetic tissue-like material that can concurrently mimic the dynamic cellular- and ECM-level behaviors has yet to be achieved. Here, we demonstrate that cellular-scale hydrated starch granules, an underexplored component in materials science, can turn conventional hydrogels into tissue-like materials when composites are formed. The composites display programmability, anisotropy, strain-stiffening, mechanochemistry, and self-healability.

Yin Fang, Endao Han, Xin-Xing Zhang, ..., Jin Wang, Heinrich M. Jaeger, Bozhi Tian

fangyin123@uchicago.edu (Y.F.)
jaeger@uchicago.edu (H.M.J.)
btian@uchicago.edu (B.T.)

HIGHLIGHTS

Granular material-based hydrogel composites display tissue-like behaviors

Synchrotron-based tools reveal the structures and dynamics of starch granules

The organization of starch granules can be mechanically programmed for memory devices

Dynamic hydrogen bonding and granular interactions are key to the tissue-like behaviors

4 **Demonstrate**
Proof-of-concept of performance with intended application/response

Fang et al., Matter *2*, 948–964
April 1, 2020
https://doi.org/10.1016/j.matt.2020.01.008

Matter

CellPress

Article

Dynamic and Programmable Cellular-Scale Granules Enable Tissue-like Materials

Yin Fang,[1,10,*] Endao Han,[1,2,10] Xin-Xing Zhang,[1,3,4,10] Yuanwen Jiang,[1,3,10] Yiliang Lin,[1] Jiuyun Shi,[1,3] Jiangbo Wu,[1,3] Lingyuan Meng,[5] Xiang Gao,[1] Philip J. Griffin,[5] Xianghui Xiao,[6,7] Hsiu-Ming Tsai,[8] Hua Zhou,[6] Xiaobing Zuo,[6] Qing Zhang,[6] Miaoqi Chu,[6] Qingteng Zhang,[6] Ya Gao,[6] Leah K. Roth,[1,2] Reiner Bleher,[9] Zhiyuan Ma,[6] Zhang Jiang,[6] Jiping Yue,[3] Chien-Min Kao,[8] Chin-Tu Chen,[8] Andrei Tokmakoff,[1,3,4] Jin Wang,[6] Heinrich M. Jaeger,[1,2,*] and Bozhi Tian[1,3,4,11,*]

SUMMARY

Living tissues are an integrated, multiscale architecture consisting of dense cellular ensembles and extracellular matrices (ECMs). The cells and ECMs cooperate to enable specialized mechanical properties and dynamic responsiveness. However, the mechanical properties of living tissues are difficult to replicate. A particular challenge is identification of a cell-like synthetic component, which is tightly integrated with its matrix and also responsive to external stimuli. Here, we demonstrate that cellular-scale hydrated starch granules, an underexplored component in materials science, can turn conventional hydrogels into tissue-like materials when composites are formed. By using several synchrotron-based X-ray techniques, we reveal the mechanically induced organization and training dynamics of the starch granules in the hydrogel matrix. These dynamic behaviors enable multiple tissue-like properties such as programmability, anisotropy, strain-stiffening, mechanochemistry, and self-healability.

INTRODUCTION

Tissues such as human skin are multicomponent and hierarchical,[1,2] mechanically heterogeneous and anisotropic,[3,4] self-healing,[5,6] impact-absorbing,[7] and dynamically responsive.[1,2,7] For example, skeletal muscle tissues can develop memories for certain movements after repetitive strength training episodes, because individual muscle fibers can actively respond to mechanical stresses through both the formation of myo-nuclei clusters and the preferred alignment of extracellular matrix (ECM)[8–11] (Figure 1A).

Traditional synthetic materials, on the other hand, do not typically possess such multiscale[12–17] and dynamic responsiveness.[18–20] Despite extensive efforts in the biomimetics field to develop ECM-like synthetic polymeric networks,[13,17,21–29] an artificial tissue-like material[30–43] that can concurrently mimic the dynamic cellular- and ECM-level behaviors has not yet been achieved.[44,45] One major challenge is developing cell-like building blocks that can display dynamic responses that are in synergy with the existing ECM-like polymer platforms.

Here, we propose that hydrated and cellular-scale granular materials can enable multiscale tissue-like behaviors in synthetic materials. Due to strong intergranular interactions, dense suspensions of granular materials dynamically respond to external stress through rapid phase transformations.[46–48] When integrated with synthetic

Progress and Potential

Biological tissues exhibit dynamic and multiscale architectures of dense cellular ensembles and extracellular matrices (ECMs). However, cell-like building blocks that display coordinated dynamic responses are hard to find, a challenge that has prevented synthetic materials from fully recapitulating tissue-like behaviors. In our work, we design a hybrid material system featuring cell-like granules embedded in ECM-like hydrogel matrices. We report that this composite readily displays tissue-like properties, including strain-stiffening, anisotropy, programmability, mechanochemistry, and self-healability. By using several *in situ* characterization tools, we attribute the tissue-like behaviors to mechanically induced organization of the starch granules in the hydrogel matrix. The fundamental insights gleaned from our study could also promise future development of adaptive metamaterials used for switches, sensors, actuators, and robotics, whose functions can go beyond those of natural systems.

hydrogel networks (Figure 1B), the grain-embedded composite could be considered an analog of biological tissue in terms of both structures (hierarchical assembly of cell and ECM) (Figure S1) and properties (such as dynamic responsiveness and remodeling, and memory effect). To demonstrate proof of concept, we use hydrated starch granules (Figures 1C–1E) as the model system because their grain size is similar to the size of single cells. We use a mixture of polyacrylamide (PAA)/alginate (Alg) as the matrix (Figure 1C) because this mixture yields ECM-like viscoelasticity.[27,49,50]

RESULTS AND DISCUSSION

Starch Granule-Embedded Hydrogels

To prepare the granule-embedded composites, we adopted a common thermal-initiator-induced radical polymerization method. We vigorously mixed an aqueous suspension of prehydrated wheat starch particles with monomers (i.e., acrylamide and Alg) and gelled the entire mixture in a casting mold upon thermal decomposition of the polymerization initiator ammonium persulfate (Table S1). After gelation, starch granules are effectively confined within a shape-controlled polymeric network, unlike the originally aqueous suspension that is a fluid under low applied stress.

We first studied several static structural and mechanical properties of the composite and found that our synthetic starch-in-hydrogel system shares several common features with a natural cell-in-ECM system. Similar to the ECM structures in living tissues (Figure S1), the matrix of the composite shows a nanostructured network (Figure 1C). The cellular-scale starch granules have an average grain size of ~11 μm (Figures 1D and 1E). They are evenly distributed and form tight bonding at the interfaces with the nanostructured hydrogel network (Figures 1C and S2). *In situ* X-ray scattering of the composite showed that the starch granules are fully hydrated (Figure S3), a feature other granules such as silica oxide or resin particles find difficult to acquire. In general, the hydrogel composites exhibited a Young's modulus ranging from tens of kPa to hundreds of kPa, which is comparable with that of soft tissues (i.e., 1–500 kPa, Figure S1).

Triggered Organization and Relaxation Dynamics of Starch Granules

After setting up the starch-in-hydrogel system, we studied how individual starch granules behave under external stimuli. In aqueous starch suspensions, granular packing plays a crucial role in determining the viscosity and shear modulus (when jammed).[46–48,51] Consequently, in the hybrid gel, we expected the spatial distribution of the starch particles to be critical in determining the hydrogel mechanics. By introducing two *in situ* visualization methods with X-ray, we studied (1) the static configuration of the particles when the hybrid gel was deformed to a certain strain and reached a steady state and (2) the transient relaxation process directly after the deformation, when the reconfiguration of the particles was still going on.

X-ray micro-computed tomography (CT) allowed us to directly visualize the static three-dimensional (3D) arrangement of starch granules with a 1.3-μm spatial resolution (Figure 2A). To highlight the features in spatial distribution of the particles, instead of using the reconstructed images in real space (Figures 2B and S4) we looked at the reciprocal space (i.e., *k*-space) with 3D fast Fourier transform (FFT). In Figure 2C, we present the two-dimensional (2D) FFT patterns by averaging the 3D results azimuthally around the stretching direction ***z***. In a pristine hybrid gel with a 35% starch content and no stretching history, the 2D FFT pattern was a featureless circular ring (Figure 2C, left panel), indicating that the initial distribution of starch granules was random and isotropic. As the strain was increased, the

[1]The James Franck Institute, University of Chicago, Chicago, IL 60637, USA

[2]Department of Physics, University of Chicago, Chicago, IL 60637, USA

[3]Department of Chemistry, University of Chicago, Chicago, IL 60637, USA

[4]The Institute for Biophysical Dynamics, University of Chicago, Chicago, IL 60637, USA

[5]The Pritzker School of Molecular Engineering, University of Chicago, Chicago, IL 60637, USA

[6]Advanced Photon Source, Argonne National Laboratory, Lemont, IL 60439, USA

[7]National Synchrotron Light Source II, Brookhaven National Laboratory, Upton, NY 11973, USA

[8]Department of Radiology, University of Chicago, Chicago, IL 60637, USA

[9]Department of Materials Science and Engineering, Northwestern University, Evanston, IL 60208, USA

[10]These authors contributed equally

[11]Lead Contact

*Correspondence: fangyin123@uchicago.edu (Y.F.), jaeger@uchicago.edu (H.M.J.), btian@uchicago.edu (B.T.)

https://doi.org/10.1016/j.matt.2020.01.008

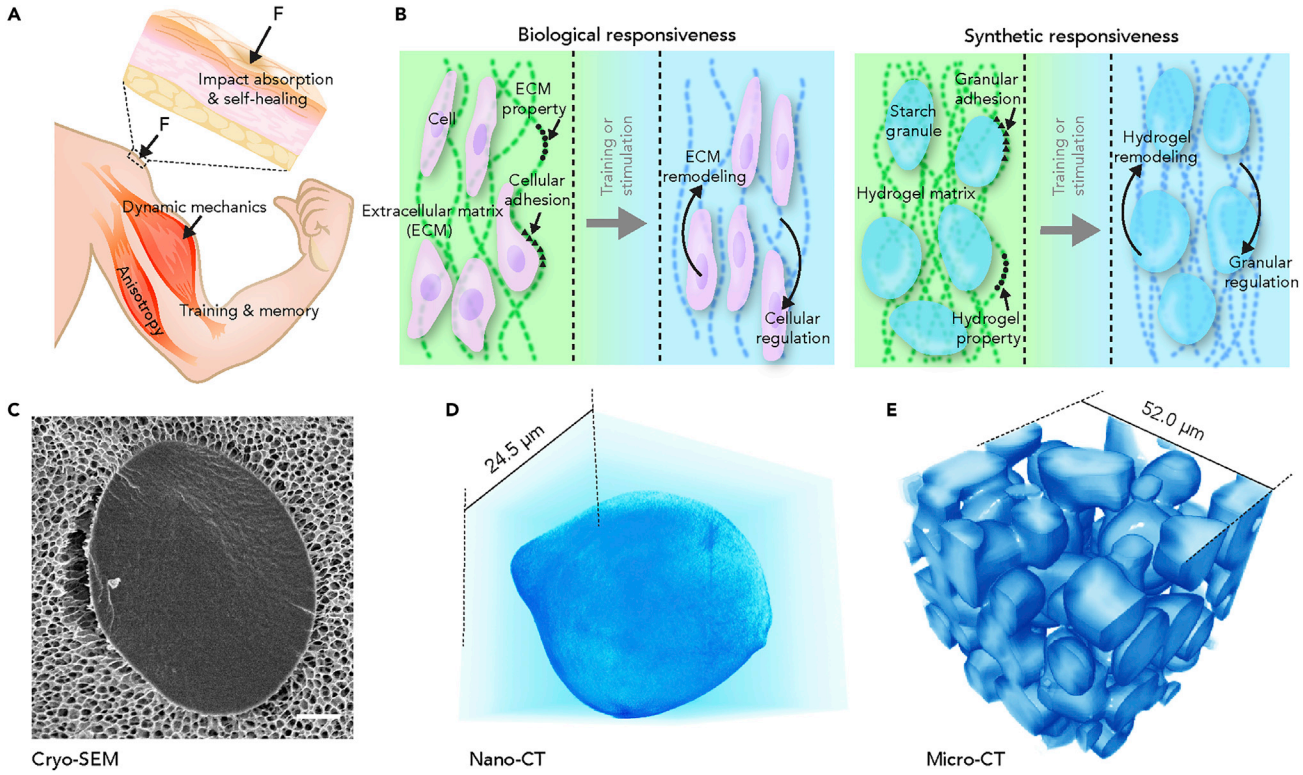

Figure 1. Granular Composite for Tissue-like Materials

(A) Biological tissues (e.g., skeletal muscles) can develop memories and respond actively to mechanical stresses.

(B) Starch granule-embedded hydrogel composite can be an analog of biological tissues in terms of both the structures (i.e., hierarchical assembly of cell and ECM) and properties (i.e., dynamic remodeling and regulation after training or stimulation).

(C) Cross-sectional cryo-scanning electron microscopy image showing the seamless integration between the starch granule and the surrounding polymeric matrix. Scale bar, 1 μm.

(D and E) Reconstructed X-ray tomography data from a hydrogel composite showing the irregularly shaped single particle (nano-CT, [D]) and particle-particle contacts (micro-CT, [E]).

originally uniform distribution evolved into an elliptical pattern with a gap at k_z = 0 and two discontinuous arcs (Figure 2C). When the strain level reached a critical point (i.e., ~100%), another gap appeared at k_r = 0 that further separated the two arcs into four symmetrical islands (the two rightmost arcs are shown in Figure 2C). These hot spots centered at (k_r*, k_z*) with the k_z*/k_r* ratio asymptotically approaching a constant value | k_z*/k_r* | ≈ 0.8 (Figure 2C) until the strain reached ~500%. When the initial starch packing fraction was low, the transition at ϵ = 100% was not pronounced during stretching (Figure S5). This means that at maximum strain (ε_{max}), the average intergranular distance was elongated along the extension direction ***z***, i.e., l_z increases (Figures 2C–2E). Meanwhile, denser structures of starch granules were formed along the ***r*** direction, i.e., l_r decreases, which is consistent with the overall deformation of the hydrogel composite with a positive Poisson's ratio (Figure S6). At the beginning of the second stretching (Figures 2C and 2D) or when the first stretching was over, i.e., at 0% strain, k_z*/k_r* ≈ 1.8, which suggests that after a full cycle, the characteristic length scales in the granular packing are reduced along the direction of the stretching and elongated perpendicularly. Such a sharp transition indicates that strain can trigger granular motion inside the viscoelastic PAA-Alg matrix. After the second stretch, no sharp transition of microstructural reorganization was observed (Figure S7), because the granular particles were already prealigned after the first cycle (Figure 2E).

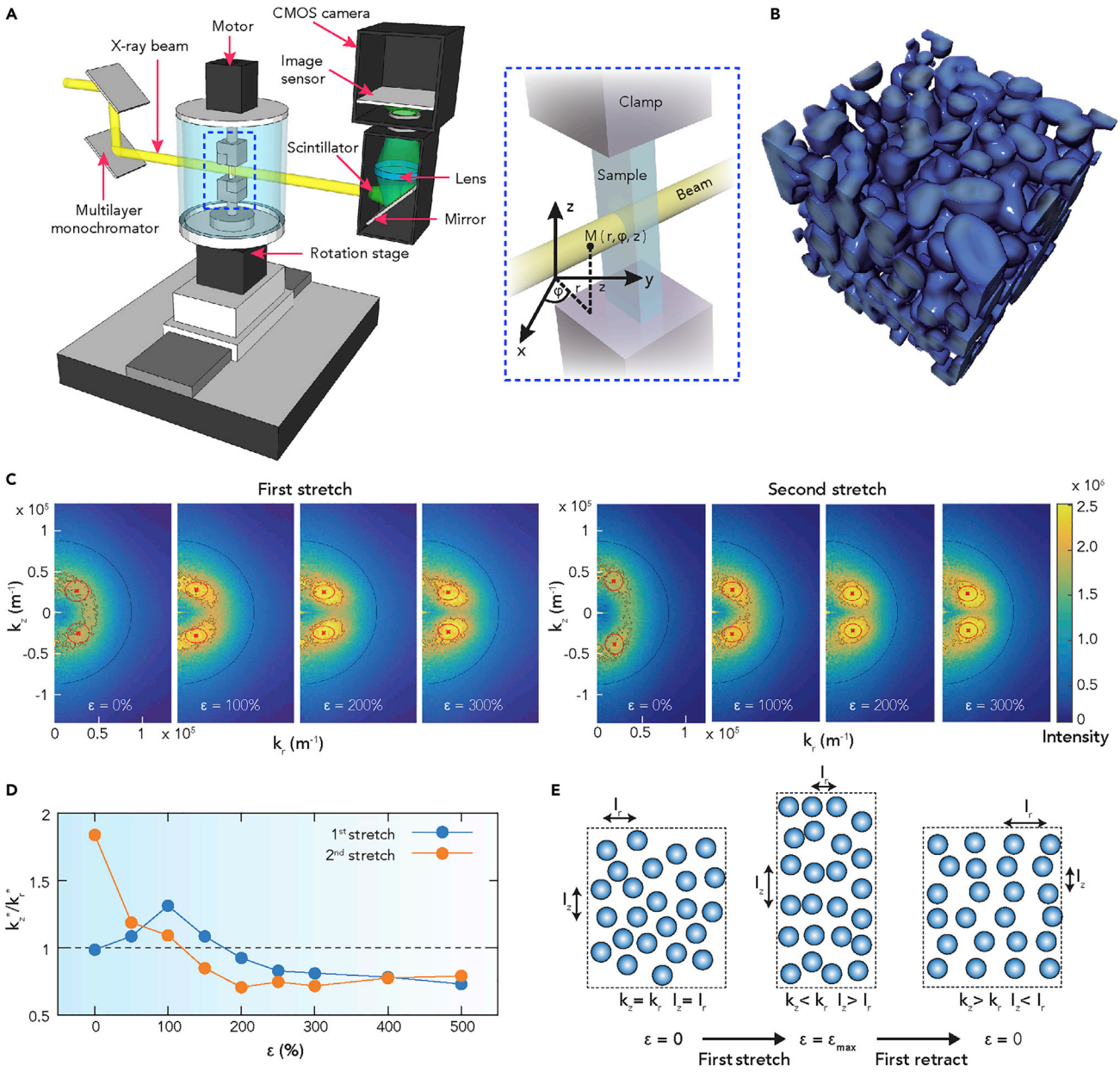

Figure 2. Strain Can Organize Starch Granules in Hydrogel Matrix

(A) Schematic of the X-ray micro-CT setup showing the relative orientation of the sample, X-ray beam, and clamps that hold and stretch the hydrogel sample.

(B) Three-dimensional (3D) reconstructed image of the spatial distribution of starch granules in the hydrogel composite at 500% strain.

(C) Two-dimensional (2D) fast Fourier transform (FFT) spectra of X-ray images from the same hydrogel composite under different strains during the first and second stretching processes. Black circles, spatial frequency corresponding to the average particle diameter of 11 μm; red circles containing crosses, weighted mean positions of starch granules in the reciprocal space.

(D) Evolution of starch distribution as a function of strain. The center position changes of the hot spots (red crosses marked in [C]) at different strain levels in the first and second stretching cycles were analyzed and plotted.

(E) Schematic of starch granules in hydrogel composite showing the microscopic alignment under global mechanical manipulation.

To understand the particle relaxation dynamics on the similar temporal scale of the stretching process, we employed X-ray speckle correlation spectroscopy (XSCS). This method allowed us to image a 2D projection of the 3D structure at a much higher temporal resolution in comparison with the CT. In this experiment, a hydrogel

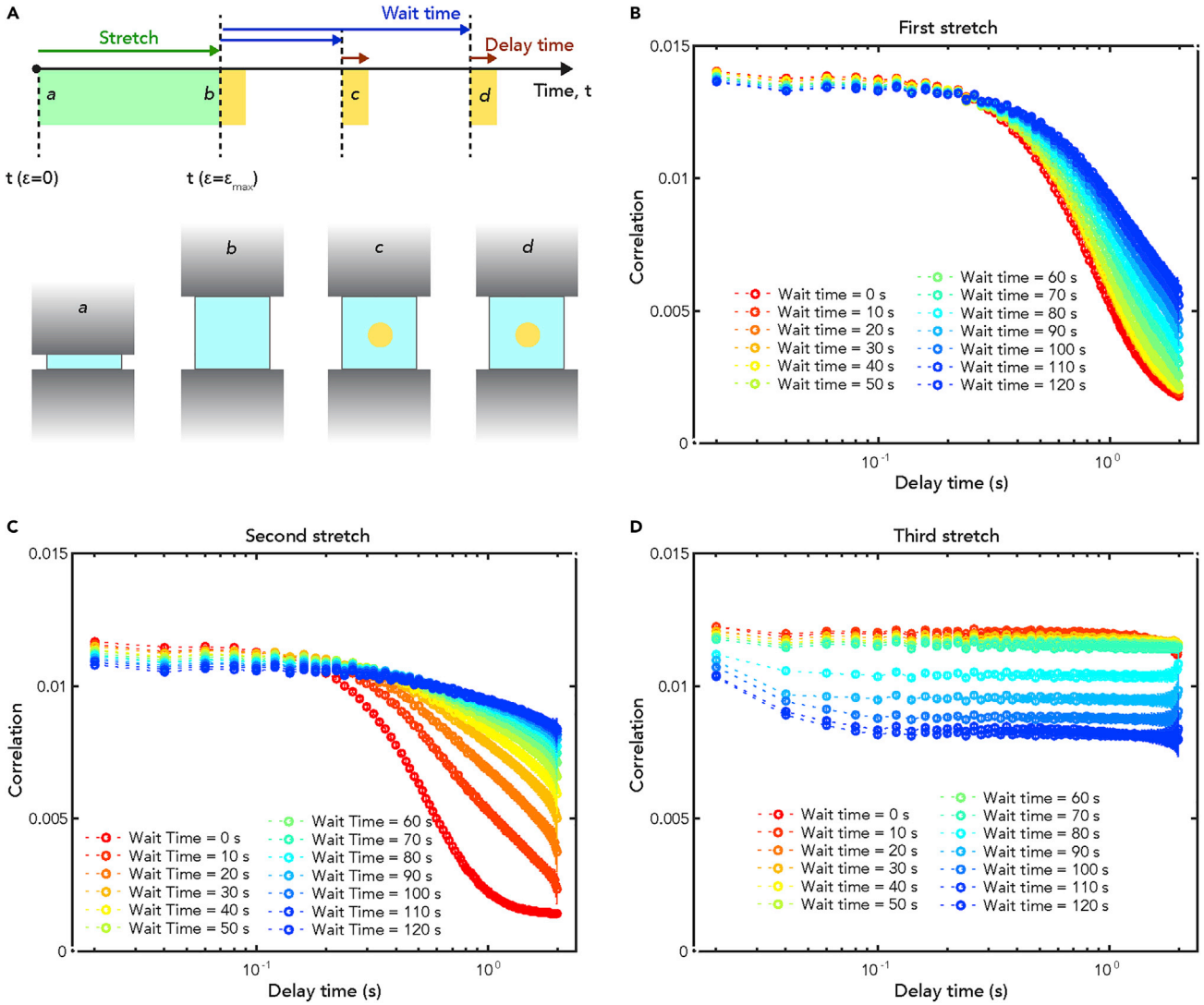

Figure 3. X-Ray Speckle Correlation Spectroscopy Characterizes the Motion Relaxation Dynamics of Starch Granules in Hydrogel Composite

(A) Schematic diagram illustrating the experimental protocol. A hydrogel sample was stretched three times, and the granular relaxation dynamics were probed (yellow areas) immediately after each stretching process with X-ray photon correlation spectroscopy.

(B–D) The correlation function calculated from near-field, transmission geometry X-ray scattering intensities after the first stretch (B), second stretch (C), and third stretch (D) while the sample is held stationary by the clamps. Each measurement lasted for approximately 120 s. The relaxation of the starch grains immediately after the stretching results in significant rearrangement and dislocation of the particles within a 120-s time window, but then become almost completely arrested within similar time windows with consecutive stretches.

sample was stretched three times while keeping the maximum strain constant, and we recorded the relaxation dynamics of the starch immediately after the hydrogel reached the maximum strain (Figure 3A). The starch granules displayed persistent motions within the polymeric matrix for at least 120 s after the first stretch (Figure 3B). The motions were less pronounced after the second stretch (Figure 3C) and were negligible after the third stretch (Figure 3D). The relaxation dynamics from the XSCS studies are consistent with the coherent X-ray scattering images (Figure S8) and the static X-ray CT results (Figure 2), highlighting that the initial stretch is critical to programming the granular structures within the hydrogel matrix. The arrest of the relaxation dynamics after the second stretch suggests that mechanical programming of the hydrogel composite only requires 1–2 cycles of training.

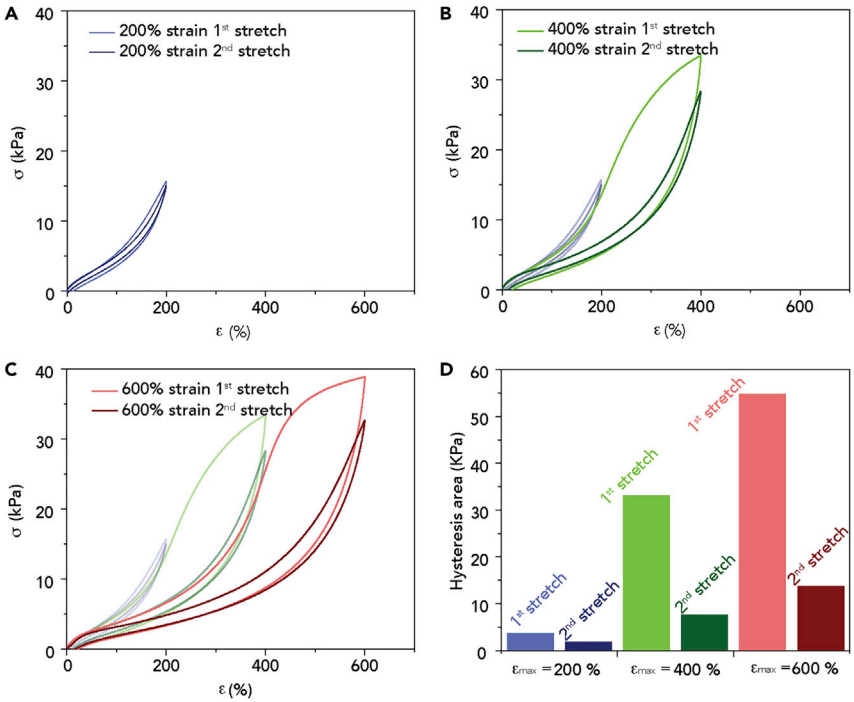

Figure 4. Mechanical Training Produces Strain-Dependent Mechanical Properties in the Composites

(A–C) The energy dissipation capability of the hydrogel composite is dependent on its history of external stress. After the first loading/unloading cycle to a certain strain, the gel consistently showed significantly reduced hysteresis in the second cycle to the same strain level. In addition, the hysteresis area remained low before the previous maximal strain level but became much larger afterward. Maximal strain levels: 200% (A), 400% (B), 600% (C).

(D) Analysis of the hysteresis areas showing the history-dependent energy dissipation.

Mechanical Memory Effect

From the X-ray tomography data, we observed the memory in particle configurations after training the sample beyond a threshold strain. Here, we show that strain-induced reorganization of starch granules within the hydrogel matrix correlates strongly with the mechanical properties of the composites.

In two loading/unloading cycles to the same maximum strain level, the hybrid gel consistently showed significantly reduced hysteresis in the second cycle in comparison with the first cycle (Figures 4A–4C and S9). With further repetitive cycles, the hysteresis area stabilized at the low level over the next 49 runs (Figure S9). This strain history-dependence is similar to the Mullins effect discovered in filled rubbers.[52,53] The hysteresis during a loading/unloading cycle reflected an energy dissipation, likely due to reconfiguration of the granules and breaking of bonds between the granules and the gel network. When we increased the maximal strain, the stress-strain curve showed different trends before and after the previous maximal strain point (Figures 4B and 4C). Specifically, the hysteresis area remained low before the previous maximal strain level but became much larger afterward (Figures 4A–4C). This observation indicates that the energy dissipation capability of the starch hybrid gel is dependent on its history of mechanical training. Additionally, comparison of the second loading/unloading cycles recorded with different maximum strains (i.e., 200% strain second stretch in Figure 4A, 400% strain second stretch in Figure 4B, and 600% strain second stretch in Figure 4C) highlights that the hydrogel

composite becomes generally softer if the maximum strain applied for the first cycle (i.e., 600%) is larger (Figure 4D).

Interestingly, in both particle configuration (microscopic) and stress-strain responses (macroscopic), we observed a threshold strain beyond which the material started to display the memory characteristics. For the composite with 35% starch content, this threshold strain is approximately 100%. Below this strain, the hysteresis area enclosed by a stress-strain loop is small (Figures 4A and S10), and the second loop is close to the first loop in shape and enclosed area. The hysteresis increased dramatically when the applied strain exceeded this threshold; as described above, this irreversible training process leads to a softer, less dissipative material. We argue that the underlying mechanism of this memory effect is the non-affine reconfiguration of the particles due to direct particle-particle interaction under large deformation of the material. This effect has been studied in particulate suspensions under periodic shear,[54–56] whereby a critical strain is determined. One major difference between these two systems is that in the suspensions, the reversibility is due to the symmetry of flow at low Reynolds number, whereas in the hydrogel composite it is due to the elasticity of the hydrogel matrix. At the same time, due to hydrogen bonding between the starch granules and the hydrogel matrix (discussed later), reconfiguration of particles causes significant energy dissipation even though the hydrogel matrix is elastic.

Reprogramming and Control of Microstates

We next explored the possibility of reprogramming and modulating granular microstates inside the hydrogel matrix. As discussed above, with non-Brownian particles in the hydrogel composites, the training is largely irreversible under thermal motion. Thus, here we employed orthogonal stretching and kneading to reprogram the microstates for starch granules (Figure 5A). We investigated three macroscopic mechanical responses: the first stretching cycle, which we considered "WRITE;" further stretching along the same direction after the first cycle to access the memory retention; and stretching along an orthogonal direction, which we considered "OVERWRITE."

Due to the substantial starch reorganization, the first stretch-and-release cycle of a hybrid gel typically dissipated the largest amount of energy (Figures 5B and S10–S13). Subsequent stretching cycles consistently produced much smaller hysteresis areas that were largely overlapping (Figures 5B and S13), suggesting that starch grains were already mechanically trained in a defined state after the first stretching cycle (i.e., "WRITE" operation). However, after rotating the sample by 90° and stretching it in an orthogonal direction, the hydrogel composite showed a pronounced hysteresis area recovery (Figures 5B and S10–S13). Further stretching in the same 90° direction only yielded small hysteresis areas (Figures 5B and S10–S13). Likewise, the hysteresis area can be restored by stretching at 180° relative to the initial direction (Figures 5B and S10–S13). Essentially, we were able to modulate the energy dissipation of the gel simply by controlling the stretching direction, i.e., the gel can be regarded as a mechanical memory device whose energy dissipation level reflects its history (Figure 5B). Finally, randomly applied strains obtained by kneading the sample can rejuvenate the gel (i.e., "ERASE" operation) and recover its ability to dissipate the maximum energy by resetting the starch organization (Figures 5A and S14).

To further demonstrate the controllability of such a mechanical memory device, we studied the dependence of the hysteresis area on the applied strain. We used the hysteresis area during the first cycle at 90° (i.e., $S_{90^\circ,\mathrm{first}}$) as the reference area. With

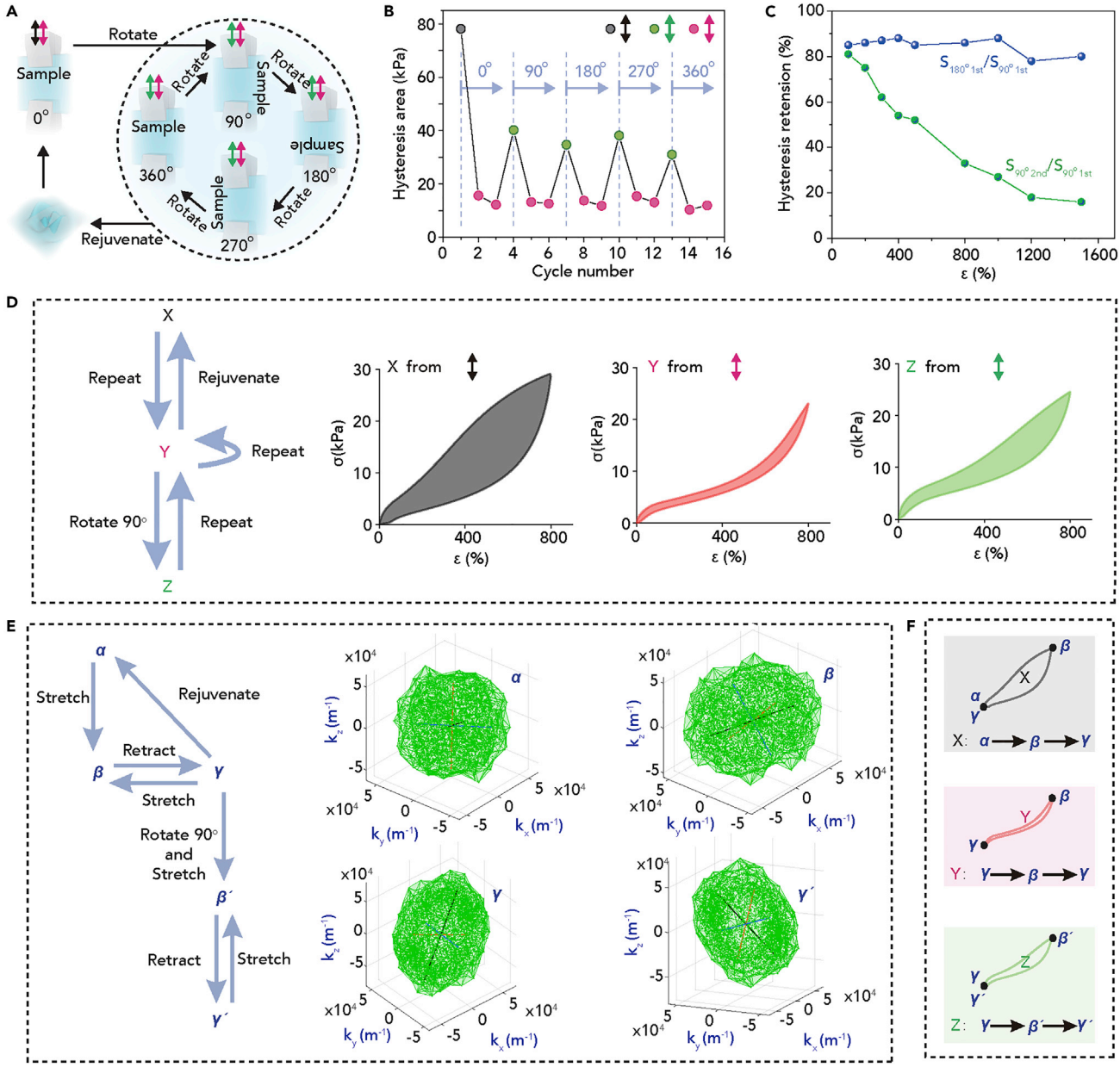

Figure 5. Mechanically Trained Starch Granules Enable Reprogrammability

(A) Schematic of basic reconfiguration steps for the hydrogel composite. Two-way arrows represent stretch/relax cycles. Black arrows represent the first cycle on a pristine sample. Pink arrows represent subsequent cycles along the same direction. Green arrows represent the first cycles after each 90° rotation. Blue one-way arrows denote other steps between stretch/relax cycles, such as rotating and kneading. Color coding remains the same throughout this figure.

(B) Energy dissipation, as manifested by the hysteresis area, in a starch hybrid gel changes according to rotation of stretching directions. Sample was stretched to ε = 800% in each cycle.

(C) Quantitative analysis of the gel memory effect with respect to strain level. Data from the first and second cycles after 90° rotation ($S_{90°,first}$ and $S_{90°,second}$, respectively) and the first cycling after 180° rotation (i.e., $S_{180°,first}$) were analyzed.

(D) Macroscopic responses of the mechanical memory device and corresponding stress-strain curves.

(E) Microscopic states of the starch granules based on 3D FFT patterns of particle configurations from the X-ray micro-CT data.

(F) Macroscopic responses and microscopic structures are correlated.

increasing strain (ϵ), the $S_{90°,second}/S_{90°,first}$ ratio decreases (Figure 5C). This suggests that the one-time "WRITE" is more pronounced at higher ϵ, consistent with the strain-dependent granular organization (Figures 5C and S10–S13). Nevertheless, ϵ does not significantly affect the $S_{180°,first}/S_{90°,first}$ ratio (Figure 5C), suggesting that the reorganization of starch granules along an orthogonal direction (i.e., "OVER-WRITE" operation) can still be effective even though the prior "WRITE" is enforced by a larger ϵ.

Figure 5D summarizes our results for the three macroscopic mechanical responses encoded by the granular motion and patterning: ***X*** (the first stretching cycle) during "WRITE," ***Y*** (further stretching along the same direction after the first cycle) to access the memory retention, and ***Z*** (stretching along an orthogonal direction) during "OVER-WRITE." Additionally, kneading "ERASEs" the encoded mesoscale states of starch granules.

To connect the strain-induced evolution of the mesoscale states (Figure 2) to the macroscopic mechanical responses, we performed another set of X-ray micro-CT on the hybrid gels after orthogonal stretching (Figures 5E and S15). The as-made starch-filled hydrogel sample was in an isotropic state (α). During the first stretching, an asymmetric state (β) in the ***k***-space formed and followed the overall shape change of the hybrid gel, which exerted an ellipsoidal 2D Fourier diffractogram that elongated in the ***r*** direction (Figure 5E). The γ state was obtained after the unloading process, which was also anisotropic, but the long axis was aligned along the ***z*** direction (Figures 5E and 2C). Interestingly, subsequent X-ray tomography of the starch distribution during stretching in other directions revealed the existence of more intermediate states of β' and γ', which partially resembled the anisotropic features of β and γ but with slightly less pronounced asymmetry (Figure S15). Figure 5F summarizes the general working flow that guides the operation of our mechanically encoded memory device using these basic mesostructural building blocks (Figure 5E, left).

Strain-Stiffening

From Figures 2 and 4, we can see that reorganization of the starch granules results in changes in the mechanical properties of the composite. Accurate measurement of the Young's modulus or the shear modulus of soft materials (such as the hydrogel composite) is not trivial. We therefore introduced ultrasound shear-wave elastography to directly measure the shear modulus G of the gel when stretched to different strains (Figures 6A–6C; Videos S1 and S2). Typically, the shear modulus of a dense starch suspension increases significantly when the starch granules are jammed.[48,51] Given the apparent alignment of the starch structures observed on the X-ray images (Figure 2C), we expected to see a similar increase in shear modulus G during hybrid gel stretching.

In the experiments with ultrasound, we pushed a transducer against the bottom surface of a stretched gel (Figures 6A and 6B) and monitored the propagation of shear waves induced by a focused ultrasound beam (Figure 6C). We extrapolated the genuine shear moduli G of individual samples, which follows $G = \rho c_s^2$, where ρ is the gel density and c_s is the shear-wave propagation speed. In agreement with the X-ray tomography and bulk tensile test (Figures 2C and S16) that showed a critical strain of ~100% at the onset of substantial starch aggregation, there was a clear inflection point near $\varepsilon = 100\%$ during the first stretching, after which the gel stiffened nearly 4-fold from 34 kPa (at $\varepsilon = 100\%$) to 113 kPa (at $\varepsilon = 200\%$) (Figure S16). Furthermore, during the second stretching process, the hybrid gel showed consistently lower values of shear moduli until the maximum strain was reached, although gradual stiffening of the gel remained evident with the increased strain level

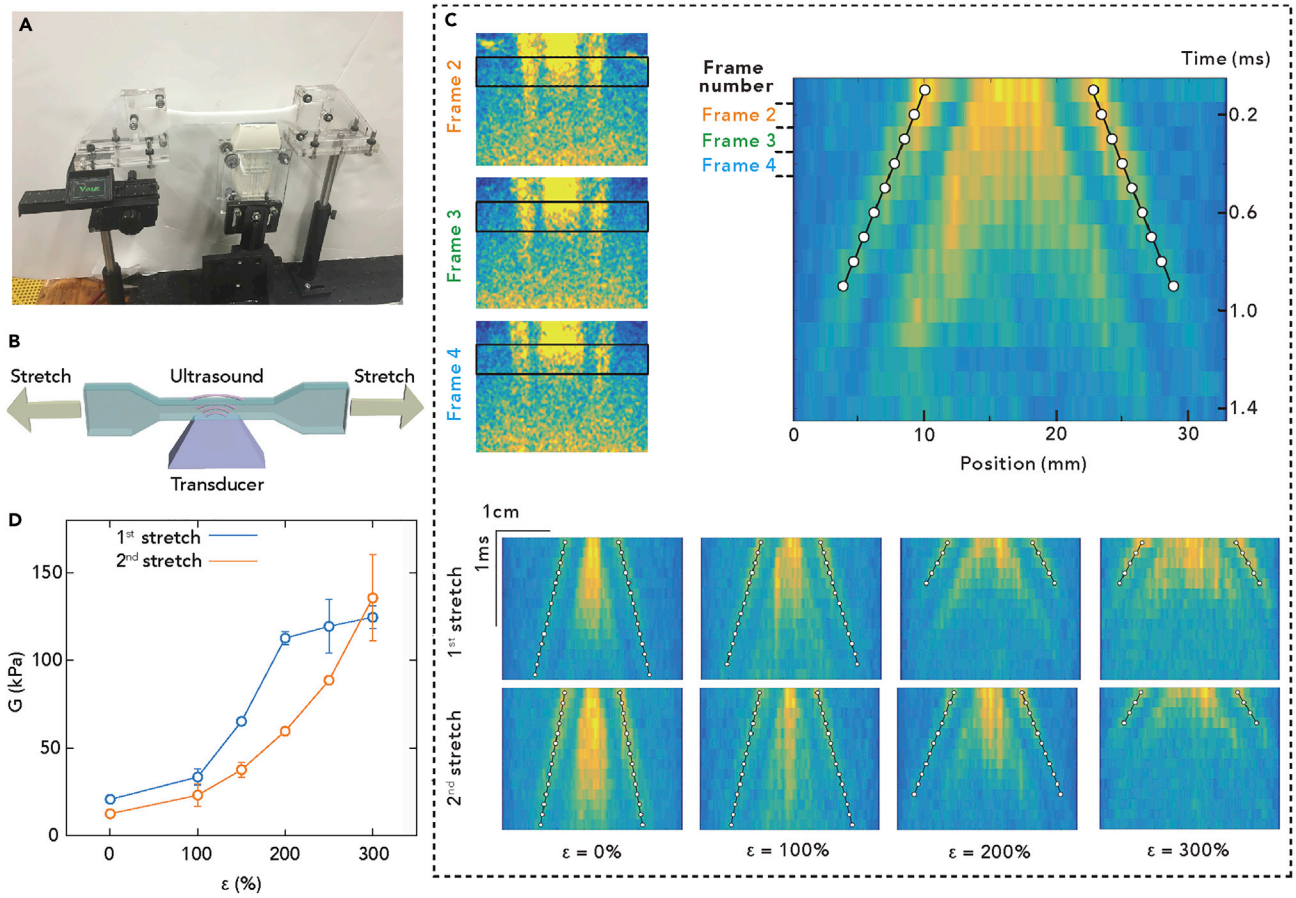

Figure 6. Characterization of the Hydrogel Composite under Mechanical Manipulation with Ultrasound Shear-Wave Elastography

(A and B) Photograph (A) and schematic (B) of ultrasound shear-wave elastography system. An ultrasound transducer was attached to the bottom of a hydrogel composite. The starch granules serve as the signal tracer and enhancer for ultrasound imaging.

(C) Propagation of shear waves on both sides of the focal point. Images were obtained by calculating the differences between in-phase and quadrature data from adjacent frames. Bright color represents regions with non-zero displacement between adjacent frames. Dashed black boxes denote areas used to generate averaged motion images for each frame. Averaged motion images from each frame were stacked together to highlight the shear-wave propagation. Positions of shear-wave fronts—one on each side of the middle focal point—are labeled with open circles. Shear-wave positions are a function of strain and time for the hydrogel composite during the first and second stretching processes. Each panel is an average over three repeated measurements.

(D) Shear moduli calculated from shear-wave speeds at different strains for two stretching cycles. Three measurements were performed at each strain for statistical analysis. Open circles represent mean values of the shear modulus. Error bars denote standard deviations.

(Figure S16). Collectively, these characterizations once again demonstrate that strain-induced reorganization of the starch granules correlate strongly with the macroscopic mechanical properties of the hydrogel composite.

Enhanced Toughness, Self-Healing, and Mechanochemistry within the Composite

In the preceding sections, we focused on a few critical tissue-like features, e.g., the programming and reprogramming of the granular states in hydrogel matrix, as well as their effects on the mechanical properties of the composites. In this section, we will discuss other aspects of the tissue-like materials.

First, we measured the toughness of different hydrogel composites via tensile tests (Figure 7A). Although the starch hybrid gel has a tissue-level Young's modulus, which is in the range of tens of kPa, its stretchability is much higher than that of normal

biological tissues (~7,900% for the gel versus ~110% for skin). To dissect how the starch granules and polymeric network composition enable this high toughness, we conducted tests on different control samples (Table S2). Upon addition of increased concentrations of urea—a known disruptor of hydrogen bonding[46]—to the hybrid gel, we observed that the stretchability and toughness of the gel progressively decreased[57] (Figures 7A and S17). In the absence of starch, the PAA-Alg hydrogel had much less stretchability than the hybrid gel (Figures 7A, S17, and S18). Both the fracture strain and the Young's modulus of the hybrid gel increased with higher loadings of starch granules (Figure S19). When we replaced the starch with microparticles of silica (SiO_2), a structural analog with dimensions similar to those of the starch grains but with chemical and mechanical differences, the stretchability of the gel composite was greatly compromised (Figure 7A). Moreover, when Alg was removed from the matrix, the fracture strain of the hydrogel composite dropped from ~7,900% to ~4,090% (Figure 7A). Alginate dispersion within the PAA could have lowered the overall crosslinking density of the hydrogel matrix and thus enhanced the granular organization, as evidenced by the decreased Young's modulus (36 kPa versus 75 kPa; Figure S17) and enhanced viscoelastic behaviors (Figures S20 and S21) when Alg was incorporated into the hydrogel composite.

To further understand the molecular picture behind the toughness of the hybrid gel, we performed attenuated total reflectance Fourier transform infrared spectroscopy of the gel under strain (Figure 7B, detailed in Figure S22). Notably, in addition to the main absorption peak (1,637 cm^{-1}) of PAA, two shoulder peaks (1,606 and 1,674 cm^{-1}) started to emerge as the strain amplitude increased (Figure 7B). These shoulder peaks were assigned to the sheet-like structures between the side chains of PAA due to chain alignment under stretching. Control experiments on a SiO_2-embedded gel (Figure S23) or pure PAA-Alg showed much fewer changes during stretching. *In situ* X-ray scattering confirmed that the intrinsic starch structure was unaltered during stretching (Figure S24). These observations suggest that, in the presence of starch granules, the interchain hydrogen-bonding network could have been enhanced during the stretching process. Given that the applied strain increases the strength of hydrogen-bond network through granule-enabled strain "focusing,"[58] the results suggest an approach for mechanochemical modulation of hydrogel matrix and are reminiscent of the ECM remodeling in biological tissues (Figure 1B).

Given the existence of dynamic hydrogen bonds in the hydrogel composites, we speculated that dynamic bonding could produce other effects besides strain-stiffening, such as self-healing.[59–61] To verify the self-healability of the hydrogel composites, we cut the gel and let it recover under ambient conditions. Tensile test results for the hydrogel composite showed a gradual recovery of stretchability to ~90% of its original value within 72 h after the initial cut (Figures 7C and S25). Using X-ray CT, no apparent cracks could be observed after the self-healing process (Figure 7D).

Conclusion

In conclusion, we demonstrated that granular materials, a largely ignored component of biomimetics, can be critical in enabling tissue-like behaviors in synthetic materials. The multiscale interactions between the granules and the surrounding matrix yielded a number of tissue-like properties (Figure 8 and Table S3), such as granule-triggered strain-stiffening, mechanical encoding of memory states, and enhanced stretchability and toughness in traditional hydrogels (i.e., PAA and Alg). We demonstrated that mesoscopic granular motions and actions (e.g., mechanochemical

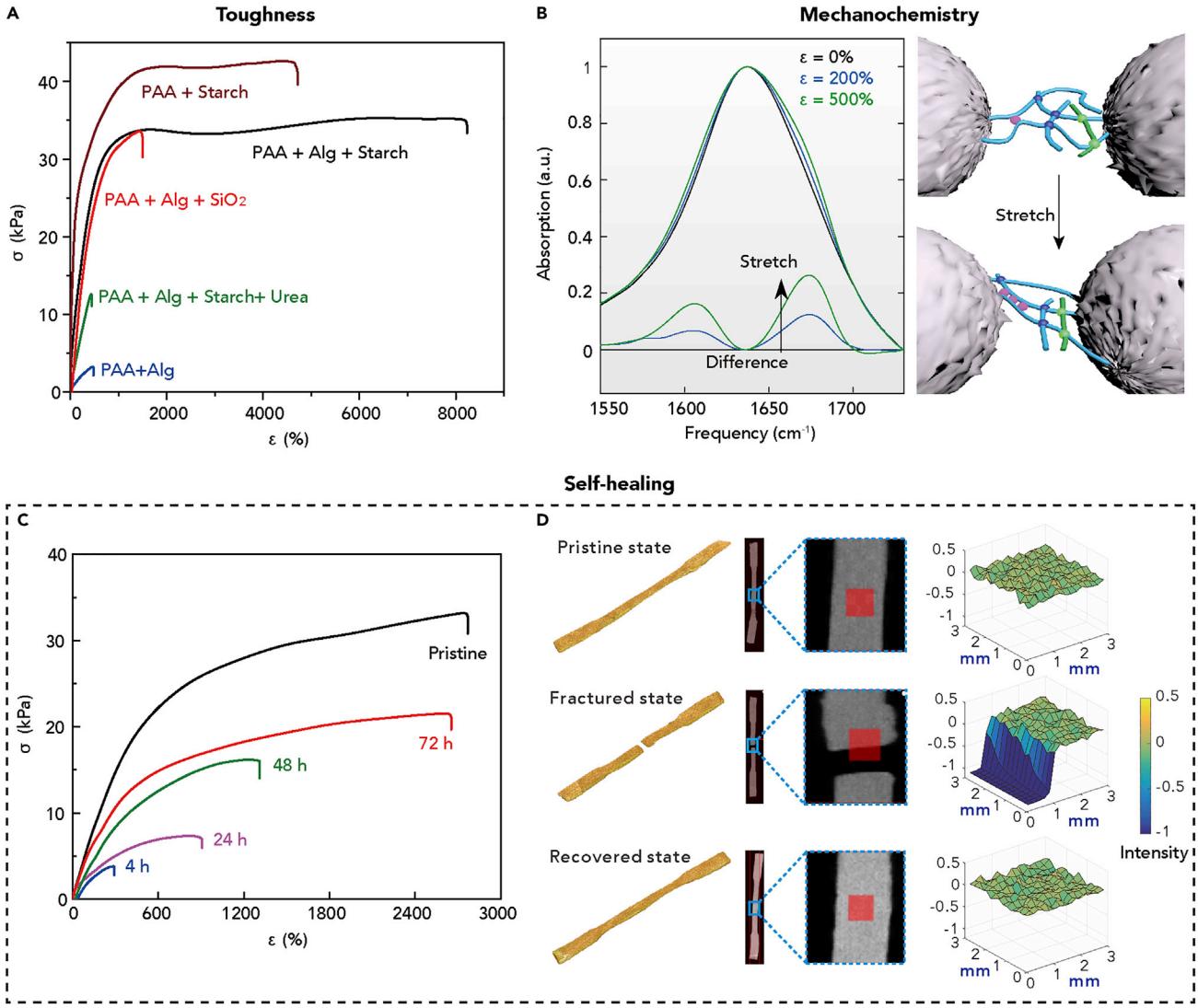

Figure 7. Starch Granules Yield Many Other Tissue-like Properties in the Hydrogel Composite

(A) Toughness. Stress-strain curves illustrate the roles of individual components in determining material stretchability. Nominal engineering stress (σ) was defined as the loading force divided by the cross-section area. Extension rates for all samples were 75 mm/min.

(B) Mechanochemistry. Left: attenuated total reflectance Fourier transform infrared spectra of the same starch-filled gel at different strain levels. Difference spectra (scale factor, 3) are plotted at the bottom with respect to the unstrained sample (black trace). Blue and green traces represent data from ε = 200% and ε = 500%, respectively. Right: schematic depicting enhancement of interchain hydrogen bonds (magenta dots) between adjacent PAA side chain (blue lines) upon stretching. The purple and green dots are the covalent crosslinking points in the PAA (blue lines) and Alg (green lines) network.

(C) Self-healing. Stress-strain curves demonstrate the self-healing behavior of the starch hybrid gel. Initial malleability and Young's modulus were gradually recovered after extended healing under ambient conditions.

(D) Self-healing. X-ray tomography data (3D volume rendering, 2D view and surface profiles) from pristine, fractured, and recovered states of a hydrogel composite (27 wt % starch in PAA + Alg). Red squares mark regions used for profile analysis.

stiffening of the hydrogel matrix) can be programmed by global mechanical manipulation. Importantly, all of these features were dependent on the presence of starch granules, i.e., they cannot be obtained with the hydrogel alone. Finally, our results suggest design considerations for metamaterials or adaptive systems[62–65] for soft robotics, bioelectronics,[38,39] and biomedical implants or delivery systems,[66,67] whose functions can go beyond natural systems.

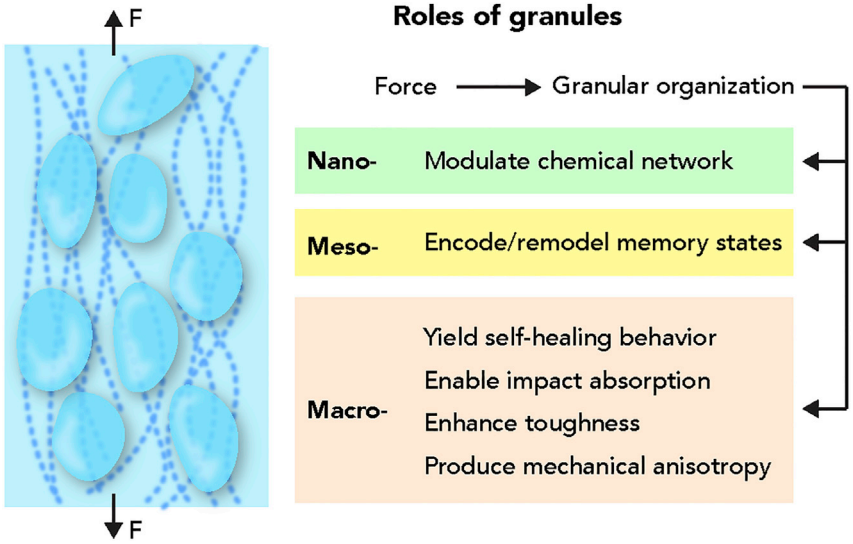

Figure 8. Summary of Key Features Enabled by Starch Granules for Tissue-like Materials
Table summarizing the key features enabled by the granular materials across multiple length scales for tissue-like materials.

EXPERIMENTAL PROCEDURES

Synthesis of Starch-Embedded Hydrogel Composites

The hydrogel composites were synthesized by mixing the composites that went along with the recipes in Table S1, and we also synthesized the several other hydrogels as control groups in Table S2.

To prepare the 43 wt % starch-filled hydrogel composite, we chose Category 1 in Table S1. First, we added the wheat starch powder (200 g) in sterilized water (250 g), and the suspension was stirred for 12 h on a hotplate with stabilized temperature and humidity controlled at 25°C to ensure the hydration of the starch particles. Alg, acrylamide (AA), ammonium persulfate (APS), and *N*,*N*′-methylene-bisacrylamide (MBAA) were then sequentially added to the suspension and stirred for an additional 48 h. Unless otherwise indicated, the weight percentage of each component used in the hybrid gel was kept as Alg (0.2 wt %), AA (3.42 wt %), APS (0.11 wt %), and MBAA (0.01 wt %). To accelerate the polymerization, we added the accelerator tetramethylethylenediamine (0.02 wt %) into the well-dispersed suspension and stirred for 2–5 min. The suspension was transferred into acrylic molds and sealed with acrylic coverslides for gelation. The hybrid gel was fully polymerized after 3–5 h.

X-Ray Tomography

The micro-CT experiments were done at the 2-BM beamline of the Advanced Photon Source at Argonne National Laboratory. The X-ray energy was set to 22 keV. The imaging device was a PCO.edge 5.5-s CMOS camera coupled with a Mitutoyo long working distance 5× lens and 20-μm-thick LuAG:Ce scintillator. A mechanical loading device with two grips was used to stretch dogbone-shaped dough samples in *in situ* micro-CT experiments. An actuator was used to adjust the gap between the two grips. The maximum travel range of the actuator is 35 mm. The tomography measurements of a sample started with the sample at rest state. The sample was then stretched step by step and scanned after each stretching step. Before a tomography scan started, the sample was relaxed for

15 min in order to reduce motions of the starch particles during the tomography scan. The loading device was completely sealed, and a piece of wet foam was placed inside to keep the sample in a 100% humidity environment. Tomography data were reconstructed with Tomopy. Single-distance phase retrieval and ring removal were performed on the raw data before tomography reconstruction. The reconstructions were done with gridrec algorithms. The reconstructed tomography data have isotropic 1.3 μm in all three dimensions. The measured volume in a single tomography scan was a cylindrical volume of 1.6 mm diameter and 1.4 mm height.

To extract information on particle configuration and orientation, we performed an FFT on the reconstructed images. First, the 2D grayscale images were combined as a 3D array, after which we applied a 3D FFT to the image array. Because the system has rotational symmetry along the extension direction ***z***, we average the 3D Fourier spectrum (k_x, k_y, k_z) in the azimuthal direction and obtain its 2D projection (k_r, k_z). To present the variation of particle configuration directly, we choose the 500 points with the highest intensity on the 2D diagram and compute their center (k_r^*, k_z^*) using intensity as weight. If $k_z^*/k_r^*<1$, the average length scale of the particle configuration is larger in the extension direction in comparison with the radial direction, and vice versa.

The nano-CT measurements were conducted with the transmission X-ray microscope at the FXI (18-ID) beamline of the National Synchrotron Light Source II at Brookhaven National Laboratory. The scan was done at 6 keV X-ray energy and a 30-nm outmost zone width zone plate. The starch particle samples were mounted on a thin Kapton tube and rotated by an air-bearing rotation stage. X-ray projection images were acquired at 14*xy* angles in 180° range. The tomography reconstruction was done with Tomopy. Single-distance phase retrieval and ring removal were performed on the raw data before tomography reconstruction. The reconstructions were done with gridrec algorithms.

X-Ray Speckle Correlation Spectroscopy

XSCS was performed at beamline 7-ID-B of the Advanced Photon Source, Argonne National Laboratory. Time-resolved X-ray speckle patterns were collected as the wide-bandpass beam from an undulator passing through the granular samples. A crystal scintillator was used to convert the X-ray speckle patterns to visible-light images, which were recorded by a high-speed camera at a frame rate of 20 kHz. The relaxation time is derived from 2D correlation of the time-resolved speckle patterns collected after each stretch.

Shear Wave Elastography with Ultrasound

Here we used a Verasonics Vantage 128 research ultrasound platform to characterize the mechanical properties of the hybrid gels via shear-wave elastography. As schematically illustrated in Figure 6B, the ultrasound transducer was pushed against the tested material and they were coupled by a layer of ultrasound gel. First, the ultrasound beam was at high power and focused to push the sample with an acoustic radiation force

$$F_{AR} = \frac{2\alpha I}{c},$$

where α is the attenuation factor in the material, I is the intensity the sound beam, and c is the speed of sound. The high-power beam was then turned off, and the ultrasound was immediately switched to the low-power imaging mode and took 500

consecutive images at 10,000 frames per second. To detect small vibrations in the sample, we calculated the difference between adjacent frames

$$\Delta I = |I_{n+1} - I_n| ,$$

where I_n is the in-phase and quadrature data of the nth frame. With ΔI, we can directly visualize propagation of shear waves and track their motion, and thus we obtain the shear modulus of the sample via Equation S2. This experimental method was calibrated with gelatin blocks.

For a complete description of the experimental procedures, please refer to Supplemental Information.

SUPPLEMENTAL INFORMATION

Supplemental Information can be found online at https://doi.org/10.1016/j.matt.2020.01.008.

ACKNOWLEDGMENTS

We thank Karen Watters for scientific editing of the manuscript. This work was supported by the US Office of Naval Research (ONR YIP, N000141612530; PECASE, N000141612958) and the National Science Foundation (NSF MRSEC, DMR 1420709). The work made use of the BioCryo facility of Northwestern University's NUANCE Center, which received support from the Soft and Hybrid Nanotechnology Experimental Resource (NSF ECCS-1542205); the Materials Research Science and Engineering Centers (MRSEC) program (NSF DMR-1720139) at the Materials Research Center; the International Institute for Nanotechnology (IIN); and the State of Illinois, through the IIN. It also made use of the CryoCluster equipment, which received support from the Major Research Instrumentation program (NSF DMR-1229693). This research used resources at the Advanced Photon Source, a US Department of Energy (DOE) Office of Science User Facility operated for the DOE Office of Science by Argonne National Laboratory under contract no. DE-AC02-06CH11357. This research also used resources at the Full-Field X-Ray Imaging Beamline at 18-ID of the National Synchrotron Light Source and a US DOE Office of Science User Facility operated for the DOE Office of Science by Brookhaven National Laboratory under contract no. DE-AC02-98CH10886. We also thank Dr. Tao Sun for providing technical support.

AUTHOR CONTRIBUTIONS

Conceptualization, Y.F. and B.T.; Methodology: Y.F., E.H., X.-X.Z., Y.J., H.M.J., and B.T.; Investigation – Experiment: Y.F., E.H., X.-X.Z., Y.J., Y.L., J.S., J.W., L.M., X.G., P.J.G., X.X., H.-M.T., H.Z., X.Z., Qing Zhang, M.C., Qingten Zhang, Y.G., R.B., Z.M., Z.J., J.Y., C.-M.K., and C.-T.C.; Investigation – Simulation: L.K.R.; Writing – Original Draft: Y.F., E.H., X.-X.Z., Y.J., Y.L., and B.T.; Writing – Review & Editing: all authors; Funding Acquisition: H.M.J. and B.T.; Supervision: A.T., J.W., H.M.J., and B.T.

DECLARATION OF INTERESTS

The authors declare no competing interests.

Received: December 18, 2019
Revised: December 30, 2019
Accepted: January 6, 2020
Published: January 29, 2020

REFERENCES

1. Fuchs, E., and Raghavan, S. (2002). Getting under the skin of epidermal morphogenesis. Nat. Rev. Genet. *3*, 199–209.
2. Simpson, C.L., Patel, D.M., and Green, K.J. (2011). Deconstructing the skin: cytoarchitectural determinants of epidermal morphogenesis. Nat. Rev. Mol. Cell Biol. *12*, 565–580.
3. Valderrabano, M. (2007). Influence of anisotropic conduction properties in the propagation of the cardiac action potential. Prog. Biophys. Mol. Biol. *94*, 144–168.
4. Cigognini, D., Lomas, A., Kumar, P., Satyam, A., English, A., Azeem, A., Pandit, A., and Zeugolis, D. (2013). Engineering in vitro microenvironment for cell bases therapies and drug discovery. Drug Discov. Today *18*, 1099–1108.
5. Dekoninck, S., and Blanpain, C. (2019). Stem cell dynamics, migration and plasticity during wound healing. Nat. Cell Biol. *21*, 18–24.
6. Li, Y.Y., Zhang, J.M., Yue, J.P., Gou, X.W., and Wu, X.Y. (2017). Epidermal stem cells in skin wound healing. Adv. Wound Care *6*, 297–307.
7. Roberts, T.J. (2016). Contribution of elastic tissues to the mechanics and energetics of muscle function during movement. J. Exp. Biol. *219*, 266–275.
8. Frontera, W.R., and Ochala, J. (2015). Skeletal muscle: a brief review of structure and function. Calcif. Tissue Int. *96*, 183–195.
9. Schoenfeld, B.J. (2010). The mechanisms of muscle hypertrophy and their application to resistance training. J. Strength Cond Res. *24*, 2857–2872.
10. Gundersen, K., Bruusgaard, J.C., Egner, I.M., Eftestol, E., and Bengtsen, M. (2018). Muscle memory: virtues of your youth? J. Phys. *596*, 4289–4290.
11. Gundersen, K. (2016). Muscle memory and a new cellular model for muscle atrophy and hypertrophy. J. Exp. Biol. *219*, 235–242.
12. Reznikov, N., Bilton, M., Lari, L., Stevens, M.M., and Kroger, R. (2018). Fractal-like hierarchical organization of bone begins at the nanoscale. Science *360*, eaao2189.
13. O'Leary, L.E.R., Fallas, J.A., Bakota, E.L., Kang, M.K., and Hartgerink, J.D. (2011). Multi-hierarchical self-assembly of a collagen mimetic peptide from triple helix to nanofibre and hydrogel. Nat. Chem. *3*, 821–828.
14. Fu, H.R., Nan, K.W., Bai, W.B., Huang, W., Bai, K., Lu, L.Y., Zhou, C.Q., Liu, Y.P., Liu, F., Wang, J.T., et al. (2018). Morphable 3D mesostructures and microelectronic devices by multistable buckling mechanics. Nat. Mater. *17*, 268–276.
15. Gantenbein, S., Masania, K., Woigk, W., Sesseg, J.P.W., Tervoort, T.A., and Studart, A.R. (2018). Three-dimensional printing of hierarchical liquid-crystal-polymer structures. Nature *561*, 226–230.
16. Rao, P., Sun, T.L., Chen, L., Takahashi, R., Shinohara, G., Guo, H., King, D.R., Kurokawa, T., and Gong, J.P. (2018). Tough hydrogels with fast, strong, and reversible underwater adhesion based on a multiscale design. Adv. Mater. *30*, e1801884.
17. Zhang, S.M., Greenfield, M.A., Mata, A., Palmer, L.C., Bitton, R., Mantei, J.R., Aparicio, C., de la Cruz, M.O., and Stupp, S.I. (2010). A self-assembly pathway to aligned monodomain gels. Nat. Mater. *9*, 594–601.
18. Cui, J.X., Daniel, D., Grinthal, A., Lin, K.X., and Aizenberg, J. (2015). Dynamic polymer systems with self-regulated secretion for the control of surface properties and material healing. Nat. Mater. *14*, 790–795.
19. Grindy, S.C., Learsch, R., Mozhdehi, D., Cheng, J., Barrett, D.G., Guan, Z.B., Messersmith, P.B., and Holten-Andersen, N. (2015). Control of hierarchical polymer mechanics with bioinspired metal-coordination dynamics. Nat. Mater. *14*, 1210–1216.
20. Hou, X., Hu, Y.H., Grinthal, A., Khan, M., and Aizenberg, J. (2015). Liquid-based gating mechanism with tunable multiphase selectivity and antifouling behaviour. Nature *519*, 70–73.
21. Kumacheva, E. (2012). Hydrogels the catalytic curtsey. Nat. Mater. *11*, 665–666.
22. McHugh, K.J., Nguyen, T.D., Linehan, A.R., Yang, D., Behrens, A.M., Rose, S., Tochka, Z.L., Tzeng, S.Y., Norman, J.J., Anselmo, A.C., et al. (2017). Fabrication of fillable microparticles and other complex 3D microstructures. Science *357*, 1138.
23. Tekin, H., Tsinman, T., Sanchez, J.G., Jones, B.J., Camci-Unal, G., Nichol, J.W., Langer, R., and Khademhosseini, A. (2011). Responsive micromolds for sequential patterning of hydrogel microstructures. J. Am. Chem. Soc. *133*, 12944–12947.
24. Yesilyurt, V., Webber, M.J., Appel, E.A., Godwin, C., Langer, R., and Anderson, D.G. (2016). Injectable self-healing glucose-responsive hydrogels with ph-regulated mechanical properties. Adv. Mater. *28*, 86.
25. Ferreira, L.S., Gerecht, S., Fuller, J., Shieh, H.F., Vunjak-Novakovic, G., and Langer, R. (2007). Bioactive hydrogel scaffolds for controllable vascular differentiation of human embryonic stem cells. Biomaterials *28*, 2706–2717.
26. Zhang, S.Y., Bellinger, A.M., Glettig, D.L., Barman, R., Lee, Y.A.L., Zhu, J.H., Cleveland, C., Montgomery, V.A., Gu, L., Nash, L.D., et al. (2015). A pH-responsive supramolecular polymer gel as an enteric elastomer for use in gastric devices. Nat. Mater. *14*, 1065.
27. Sun, J.Y., Zhao, X.H., Illeperuma, W.R.K., Chaudhuri, O., Oh, K.H., Mooney, D.J., Vlassak, J.J., and Suo, Z.G. (2012). Highly stretchable and tough hydrogels. Nature *489*, 133–136.
28. Alge, D.L., and Anseth, K.S. (2013). Bioactive hydrogels lighting the way. Nat. Mater. *12*, 950–952.
29. Lutolf, M.P., and Hubbell, J.A. (2005). Synthetic biomaterials as instructive extracellular microenvironments for morphogenesis in tissue engineering. Nat. Biotechnol. *23*, 47–55.
30. Dvir, T., Timko, B.P., Kohane, D.S., and Langer, R. (2011). Nanotechnological strategies for engineering complex tissues. Nat. Nanotechnol. *6*, 13–22.
31. Wang, S.H., Xu, J., Wang, W.C., Wang, G.J.N., Rastak, R., Molina-Lopez, F., Chung, J.W., Niu, S.M., Feig, V.R., Lopez, J., et al. (2018). Skin electronics from scalable fabrication of an intrinsically stretchable transistor array. Nature *555*, 83.
32. Chortos, A., Liu, J., and Bao, Z.A. (2016). Pursuing prosthetic electronic skin. Nat. Mater. *15*, 937–950.
33. Tee, B.C.K., Chortos, A., Berndt, A., Nguyen, A.K., Tom, A., McGuire, A., Lin, Z.L.C., Tien, K., Bae, W.G., Wang, H.L., et al. (2015). A skin-inspired organic digital mechanoreceptor. Science *350*, 313.
34. Matsuda, T., Kawakami, R., Namba, R., Nakajima, T., and Gong, J.P. (2019). Mechanoresponsive self-growing hydrogels inspired by muscle training. Science *363*, 504.
35. Yang, C.H., and Suo, Z.G. (2018). Hydrogel ionotronics. Nat. Rev. Mater. *3*, 125–142.
36. Yu, B., Kang, S.Y., Akthakul, A., Ramadurai, N., Pilkenton, M., Patel, A., Nashat, A., Anderson, D.G., Sakamoto, F.H., Gilchrest, B.A., et al. (2016). An elastic second skin. Nat. Mater. *15*, 911–918.
37. Tian, B.Z., Liu, J., Dvir, T., Jin, L.H., Tsui, J.H., Qing, Q., Suo, Z.G., Langer, R., Kohane, D.S., and Lieber, C.M. (2012). Macroporous nanowire nanoelectronic scaffolds for synthetic tissues. Nat. Mater. *11*, 986–994.
38. Yang, X., Zhou, T., Zwang, T.J., Hong, G., Zhao, Y., Viveros, R.D., Fu, T.M., Gao, T., and Lieber, C.M. (2019). Bioinspired neuron-like electronics. Nat. Mater. *18*, 510–519.
39. Webb, R.C., Bonifas, A.P., Behnaz, A., Zhang, Y.H., Yu, K.J., Cheng, H.Y., Shi, M.X., Bian, Z.G., Liu, Z.J., Kim, Y.S., et al. (2013). Ultrathin conformal devices for precise and continuous thermal characterization of human skin. Nat. Mater. *12*, 1078.
40. Song, Y.M., Xie, Y.Z., Malyarchuk, V., Xiao, J.L., Jung, I., Choi, K.J., Liu, Z.J., Park, H., Lu, C.F., Kim, R.H., et al. (2013). Digital cameras with designs inspired by the arthropod eye. Nature *497*, 95–99.
41. Lee, W.W., Tan, Y.J., Yao, H.C., Li, S., See, H.H., Hon, M., Ng, K.A., Xiong, B., Ho, J.S., and Tee, B.C.K. (2019). A neuro-inspired artificial peripheral nervous system for scalable electronic skins. Sci. Robot. *4*, eaax2198.
42. Boutry, C.M., Negre, M., Jorda, M., Vardoulis, O., Chortos, A., Khatib, O., and Bao, Z.N. (2018). A hierarchically patterned, bioinspired e-skin able to detect the direction of applied pressure for robotics. Sci. Robot. *3*, eaau6914.
43. Hamada, S., Yancey, K.G., Pardo, Y., Gan, M.Z., Vanatta, M., An, D., Hu, Y., Derrien, T.L., Ruiz, R., Liu, P.F., et al. (2019). Dynamic DNA material with emergent locomotion behavior powered by artificial metabolism. Sci. Robot. *4*, eaaw3512.
44. Prince, E., and Kumacheva, E. (2019). Design and applications of man-made biomimetic fibrillar hydrogels. Nat. Rev. Mater. *4*, 99–115.

45. Reznikov, N., Steele, J.A.M., Fratzl, P., and Stevens, M.M. (2016). A materials science vision of extracellular matrix mineralization. Nat. Rev. Mater. *1*, 16041.

46. James, N.M., Han, E.D., de la Cruz, R.A.L., Jureller, J., and Jaeger, H.M. (2018). Interparticle hydrogen bonding can elicit shear jamming in dense suspensions. Nat. Mater. *17*, 965–970.

47. Peters, I.R., Majumdar, S., and Jaeger, H.M. (2016). Direct observation of dynamic shear jamming in dense suspensions. Nature *532*, 214–217.

48. Brown, E., and Jaeger, H.M. (2014). Shear thickening in concentrated suspensions: phenomenology, mechanisms and relations to jamming. Rep. Prog. Phys. *77*, 046602.

49. Charrier, E.E., Pogoda, K., Wells, R.G., and Janmey, P.A. (2018). Control of cell morphology and differentiation by substrates with independently tunable elasticity and viscous dissipation. Nat. Commun. *9*, 449.

50. Ghosh, K., Pan, Z., Guan, E., Ge, S.R., Liu, Y.J., Nakamura, T., Ren, X.D., Rafailovich, M., and Clark, R.A.F. (2007). Cell adaptation to a physiologically relevant ECM mimic with different viscoelastic properties. Biomaterials *28*, 671–679.

51. Han, E.D., Wyart, M., Peters, I.R., and Jaeger, H.M. (2018). Shear fronts in shear-thickening suspensions. Phys. Rev. Fluids *3*, 073301.

52. Ogden, R.W., and Roxburgh, D.G. (1998). A pseudo elastic model for the Mullins effect in filled rubber. Proc. R. Soc. Lond. A *455*, 2861–2877.

53. Bueche, F. (1961). Mullins effect and rubber filler interaction. J. Appl. Polym. Sci. *5*, 271–281.

54. Corté, L., Chaikin, P.M., Gollub, J.P., and Pine, D.J. (2008). Random organization in periodically driven systems. Nat. Phys. *4*, 420–424.

55. Corte, L., Gerbode, S.J., Man, W., and Pine, D.J. (2009). Self-organized criticality in sheared suspensions. Phys. Rev. Lett. *103*, 248301.

56. Paulsen, J.D., Keim, N.C., and Nagel, S.R. (2014). Multiple transient memories in experiments on sheared non-Brownian suspensions. Phys. Rev. Lett. *113*, 068301.

57. Chen, C., Wang, Z., and Suo, Z. (2017). Flaw sensitivity of highly stretchable materials. Extreme Mech. Lett. *10*, 50–57.

58. Oosten, S.G.A., Chen, X.Y., Chin, L.K., Cruz, K., Patteson, E.A., Pogoda, K., Shenoy, B.V., and Janmey, A.P. (2019). Emergence of tissue-like mechanics from fibrous networks confined by close-packed cells. Nature *573*, 96–101.

59. Li, C.H., Wang, C., Keplinger, C., Zuo, J.L., Jin, L., Sun, Y., Zheng, P., Cao, Y., Lissel, F., Linder, C., et al. (2016). A highly stretchable autonomous self-healing elastomer. Nat. Chem. *8*, 619–625.

60. Li, J., Celiz, A.D., Yang, J., Yang, Q., Wamala, I., Whyte, W., Seo, B.R., Vasilyev, N.V., Vlassak, J.J., Suo, Z., et al. (2017). Tough adhesives for diverse wet surfaces. Science *357*, 378–381.

61. Clarke, D.E., Pashuck, E.T., Bertazzo, S., Weaver, J.V.M., and Stevens, M.M. (2017). Self-healing, self-assembled beta-sheet peptide poly(gamma-glutamic acid) hybrid hydrogels. J. Am. Chem. Soc. *139*, 7250–7255.

62. Lv, J.A., Liu, Y.Y., Wei, J., Chen, E.Q., Qin, L., and Yu, Y.L. (2016). Photocontrol of fluid slugs in liquid crystal polymer microactuators. Nature *537*, 179–184.

63. Wehner, M., Truby, R.L., Fitzgerald, D.J., Mosadegh, B., Whitesides, G.M., Lewis, J.A., and Wood, R.J. (2016). An integrated design and fabrication strategy for entirely soft, autonomous robots. Nature *536*, 451–455.

64. Kim, Y., Yuk, H., Zhao, R.K., Chester, S.A., and Zhao, X.H. (2018). Printing ferromagnetic domains for untethered fast-transforming soft materials. Nature *558*, 274–279.

65. Ma, M.M., Guo, L., Anderson, D.G., and Langer, R. (2013). Bio-inspired polymer composite actuator and generator driven by water gradients. Science *339*, 186–189.

66. Lin, X., Liu, Y., Bai, A.B., Cai, H.H., Bai, Y.J., Jiang, W., Yang, H.L., Wang, X.H., Yang, L., Sun, N., et al. (2019). A viscoelastic adhesive epicardial patch for treating myocardial infarction. Nat. Biomed. Eng. *3*, 632–643.

67. Yu, M.R., Xu, L., Tian, F.L., Su, Q., Zheng, N., Yang, Y.W., Wang, J.L., Wang, A.H., Zhu, C.L., Guo, S.Y., et al. (2018). Rapid transport of deformation-tuned nanoparticles across biological hydrogels and cellular barriers. Nat. Commun. *9*, 2607.